NANO LETTERS

Letter

pubs.acs.org/NanoLett

Tandem Solar Cells Using GaAs Nanowires on Si: Design, Fabrication, and Observation of Voltage Addition

Maoqing Yao,[†,‡] Sen Cong,[†,‡] Shermin Arab,[†,‡] Ningfeng Huang,[†,‡] Michelle L. Povinelli,[†,‡] Stephen B. Cronin,[†,‡] P. Daniel Dapkus,*[,†,‡] and Chongwu Zhou*[,†,‡]

[†]Ming Hsieh Department of Electrical Engineering, [‡]Center for Energy Nanoscience, University of Southern California, Los Angeles, California 90089, United States

Supporting Information

ABSTRACT: Multijunction solar cells provide us a viable approach to achieve efficiencies higher than the Shockley–Queisser limit. Due to their unique optical, electrical, and crystallographic features, semiconductor nanowires are good candidates to achieve monolithic integration of solar cell materials that are not lattice-matched. Here, we report the first realization of nanowire-on-Si tandem cells with the observation of voltage addition of the GaAs nanowire top cell and the Si bottom cell with an open circuit voltage of 0.956 V and an efficiency of 11.4%. Our simulation showed that the current-matching condition plays an important role in the overall efficiency. Furthermore, we characterized GaAs nanowire arrays grown on lattice-mismatched Si substrates and estimated the carrier density using photoluminescence. A low-resistance connecting junction was obtained using n^+-GaAs/p^+-Si heterojunction. Finally, we demonstrated tandem solar cells based on top GaAs nanowire array solar cells grown on bottom planar Si solar cells. The reported nanowire-on-Si tandem cell opens up great opportunities for high-efficiency, low-cost multijunction solar cells.

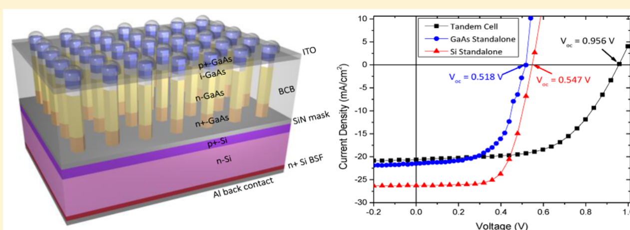

KEYWORDS: *Tandem solar cell, GaAs-nanowire-on-Si, current matching, doping characterization, heterojunction, voltage addition*

One way to surpass the Shockley–Queisser limit[1] of conventional solar cells is to employ multiple materials with different bandgaps to preferentially respond to a certain range of the solar spectrum.[2] Devices based on this concept are called multijunction solar cells. Since first introduced in the late 1970s to mid-1980s,[3,4] intense research and development on this idea has led to a surge in efficiencies.[5−7] The highest efficiencies for three and four junction solar cells under concentration have reached 44.4% and 44.7%, respectively. However, fabricating monolithic multijunction solar cells is a challenge. Lattice matching imposes a significant constraint on material choices and adds complication to the synthesis process. In lattice-mismatched metamorphic devices, the complexity in the growth of buffer layers or in the wafer peeling-off process is by no means easy. Furthermore, expensive Ge and GaAs substrates significantly increase the manufacturing cost so that the efficiency advantage is outweighed by the low cost of Si solar cells for many applications. The advancements in the understanding of nanowire material properties and device architectures provide alternative approaches.[8−15] Enhanced interaction between light and nanowires leads to efficient absorption.[11,16−22] Lattice-mismatch-induced strain can be relaxed through the nanowire sidewall.[23−27] Theoretical analysis indicates an optimal tandem cell with 1.1/1.7 eV bandgap combination can achieve efficiency higher than 40%,[28] making nanowire-on-Si heterostructures promising candidates to compete with today's three- and four-junction solar cells.

Here, we fabricated the first nanowire-on-Si tandem solar cells and observed open circuit voltage (V_{oc}) addition of separate GaAs nanowire and Si solar cells up to 0.956 V and efficiency (η) of 11.4%. Key to our success includes the design of optimal structure to achieve current matching between subcells, the epitaxial growth of the top GaAs nanowire cell on the bottom planar Si cell, and the formation of a low-resistance connecting junction between the n^+-GaAs/p^+-Si heterointerface. Our simulation indicates that GaAs nanowire length affects current matching and thus is critical to high efficiency. We also demonstrated uniform GaAs nanowire growth on lattice-mismatched Si substrate with 100% yield and developed an optical and nondestructive method to estimate the doping concentration using photoluminescence (PL). By varying the n-type dopant precursor flow rate, we were able to achieve low-resistance ohmic connecting junction between GaAs nanowire and Si subcells. The fabricated nanowire-on-Si tandem cells take advantage of the optimized parameters for each component, and their realization moves a significant step forward in low-cost and high-efficiency nanowire multijunction solar cells.

A schematic structure of the GaAs-nanowire-on-Si tandem solar cell is depicted in Figure 1. The bottom Si cells start from n-type float-zone Si substrates. p^+ emitter and n^+ back surface field are made by boron and phosphorus implantation followed

Received: May 5, 2015
Published: October 26, 2015

 © 2015 American Chemical Society

DOI: 10.1021/acs.nanolett.5b03890
Nano Lett. 2015, 15, 7217−7224

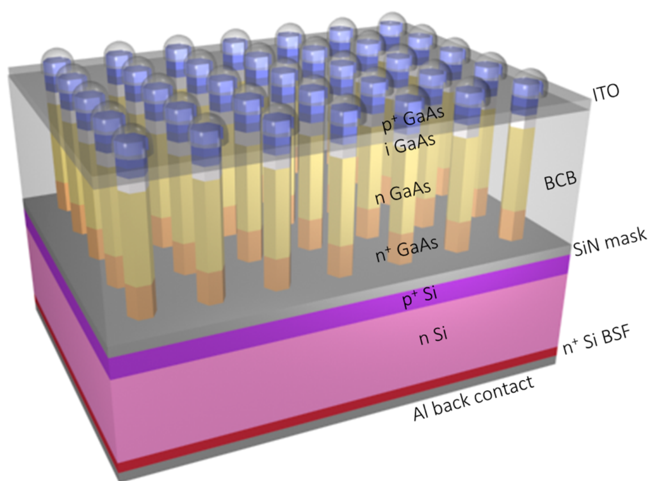

Figure 1. Schematic of GaAs nanowire-on-Si tandem solar cell. Top GaAs nanowire solar cell has p^+ emitter, undoped segment, n-type base, and n^+ root to form good connecting junction with p^+ Si. Bottom Si solar cell has p^+ emitter, n-type base, and n^+ back surface field. Nanowires are embedded in transparent insulating polymer BCB. Top contact is ITO and back contact is Al.

by rapid thermal annealing. A thin segment of n^+ doped GaAs nanowires is grown to form good connecting junction with Si. The n-type, intentionally undoped, and p-type segments are grown sequentially for the top GaAs-nanowire cell. Nanowire arrays are embedded in a transparent insulating polymer benzocyclobutene (BCB), which is etched to expose the nanowire tips. The top contact is made by a radio frequency-sputtered indium tin oxide (ITO) transparent conductive layer and the back contact is e-beam evaporated Al. For this concept of GaAs-nanowire-on-Si tandem cell to work, we need to work out the following technology components: current matching between subcells, characterization and optimization of doping in GaAs nanowires, ohmic connecting junction across n^+-GaAs/p^+-Si heterointerface, and the integration of subcells to make a functioning tandem cell. Below, we will study these components in detail.

The tandem cell should have the top and bottom cell connected in series by a low-resistance connecting junction. The smaller short-circuit current between the two subcells hence limits the output current of the tandem cell.[29] We decided the optimal structure for the tandem cell by full-vector electromagnetic simulations[30] and considered a square array of GaAs nanowires with 300 nm diameter and 600 nm pitch on a semi-infinite silicon substrate. Our previous simulation work on single-junction GaAs nanowire solar cells on GaAs substrates examines a wide range of nanowire dimensions such as diameter and pitch, and shows that this set of structural parameters (diameter of 300 nm and pitch of 600 nm) are around the optimal parameters with high optical absorption and high short-circuit current density (J_{sc}).[15] Figure 2a−c shows the simulated absorption spectra of the silicon bottom cells (red area) and the GaAs nanowire top cells (blue area) with different nanowire heights (500 nm for Figure 2a, 900 nm for Figure 2b, and 2000 nm for Figure 2c). The absorptions of the total structures are also plotted as solid black lines. Although all three structures have similar and high absorptions (>80%), the portion that the GaAs nanowires absorb becomes larger as the height of the nanowires increases from 500 to 2000 nm, which strongly affects the efficiency of the tandem cells. In Figure 2d−f, we plot the simulated current density (J) versus voltage (V) curves[1,17] for the three cases shown in Figure 2a−c. The absorption was weighted by AM 1.5 G solar spectrum[31] and the solar cells were assumed to have perfect carrier collection and no nonradiative recombination. A perfect conducting junction was assumed to connect the top and the bottom cells. For 500 nm nanowire height, the GaAs nanowire top cell can only absorb a small amount of light, and a significant portion of light with photon energy above the band gap energy of GaAs (λ < 867 nm) is transmitted through the nanowire structure and is absorbed in the silicon bottom cell. The J_{sc} of the silicon bottom cell (~23 mA/cm^2) is much higher than that of GaAs nanowire top cell (~15 mA/cm^2), which limits the total current and thus the efficiency of the tandem cell, as indicated by the black curve shown in Figure 2d. On the other hand, Figure 2e illustrates a nearly optimal case for this system. When the height of GaAs nanowire array is 900 nm, the short-circuit currents of top and bottom cells are similar, leading to the maximum overall J_{sc} of ~20 mA/cm^2. The efficiency also increases from 25.4% to 32.4% under this current-matching condition. If the height of the nanowire array further increases to 2000 nm (Figure 2f), the silicon bottom cell absorbs insufficient light and limits the overall current and efficiency. To further show the importance of current matching, we plot the short-circuit current densities of top and bottom cells (Figure 2g) and the limiting efficiency (Figure 2h) as functions of the GaAs nanowire array height. The limiting efficiency peaks at 900 nm nanowire height where the short-circuit current densities of the top and bottom cells match. We applied the optimized nanowire height of 900 nm in the experimental work described below. We note that it is also possible to achieve matched currents in the tandem cell by selecting a reasonable nanowire height and then optimizing the nanowire diameter and pitch.

GaAs nanowires used in this study were grown by selective area growth (SAG) technique using metalorganic chemical vapor deposition (MOCVD). Briefly, trimethylgallium (TMG) and arsine (AsH_3) were used as the precursors for Ga and As with partial pressures of 7.56×10^{-7} and 2.14×10^{-4} atm, respectively. Annealing in hydrogen ambient at 925 °C for 5 min was essential for high-yield vertical nanowire growth. Disilane (diluted, 100 ppm in hydrogen) was used as the precursor for Si, which is the n-type dopant for GaAs nanowires. Figure 3a−c shows the scanning electron microscopy (SEM) images of GaAs nanowires grown on Si(111) substrates. Figure 3a presents the uniformity of growth from the top-view. The yield of vertical nanowires is 100%. Figure 3b is a 30° tilted view showing the uniform wires have hexagonal cross sections enclosed by $\{1\bar{1}0\}$ facets, while Figure 3c is a magnified top-view image.

A tandem cell requires a low-resistance connecting junction (usually a tunnel junction) sandwiched by the two subcells, which can conduct current through a reverse-biased p−n junction. Typical connecting junctions require doping concentration higher than 10^{19} cm^{-3}.[32,33] Well-controlled degenerate doping in nanowires, however, presents a big challenge due to the lack of a precise doping characterization technique and the presence of surface states that reduce the effective carrier concentration.[34] Recent progress on Si/InAs nanowire heterojunction demonstrated very high current density,[35,36] indicating heavily doped III−V nanowire-on-Si heterojunction could be a viable approach to serve as the connecting junction. Previous studies relied on field effect transistor measurements

DOI: 10.1021/acs.nanolett.5b03890
Nano Lett. 2015, 15, 7217−7224

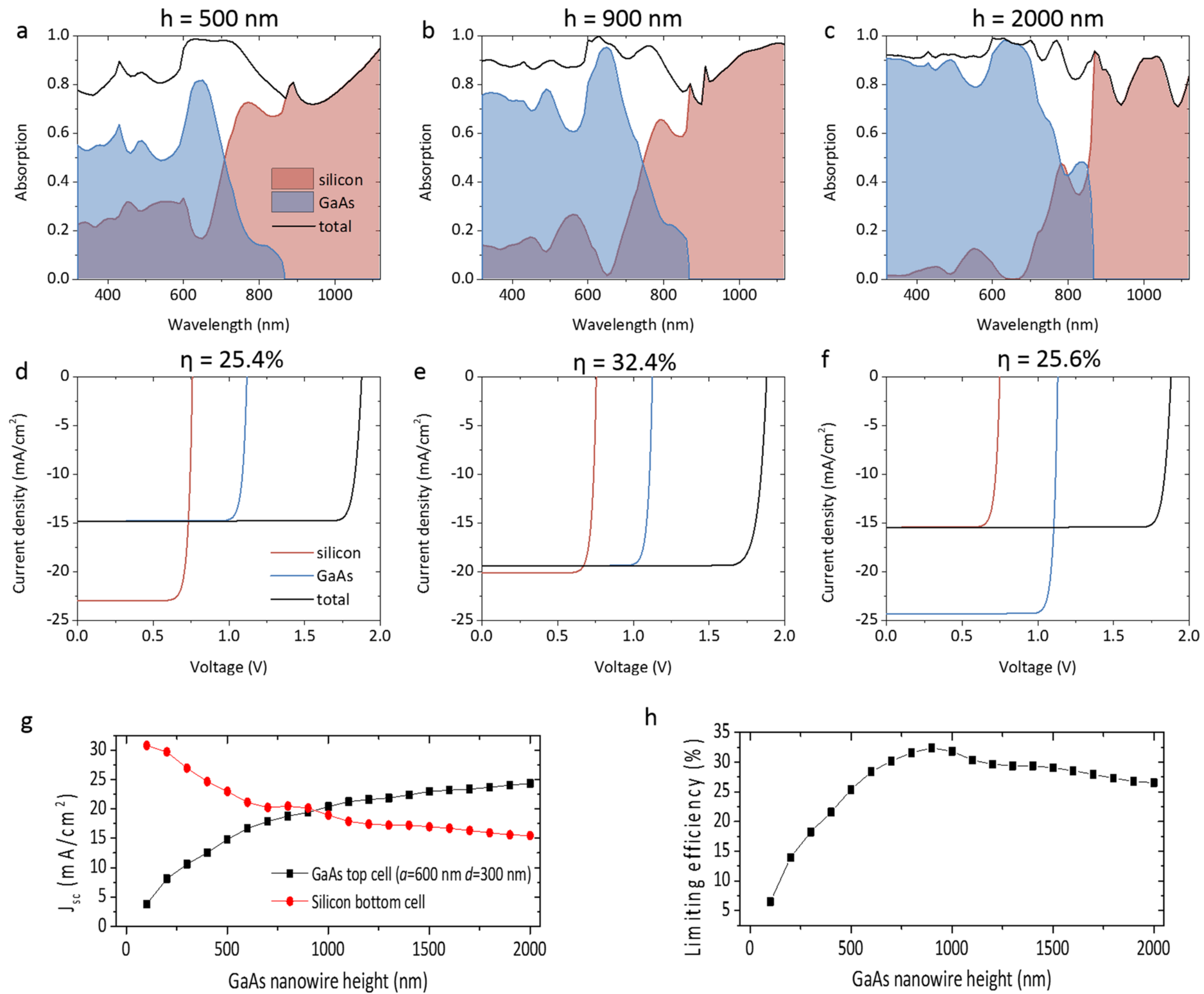

Figure 2. (a−c) Simulated absorption spectra of the Si bottom cell (red area), the GaAs nanowire top cell (blue area), and the total structures (solid black line) for nanowires with nanowire heights (a) h = 500 nm, (b) h = 900 nm, and (c) h = 2000 nm. (d−f) Simulated corresponding J−V curves, which show nearly matched currents between GaAs and Si for (e) the optimized height with h = 900 nm, and mismatched currents for (d) shorter nanowires with h = 500 nm and (f) taller nanowires with h = 2000 nm. (g) The simulated J_{sc} in the top GaAs nanowire cell and the bottom silicon cell as functions of the nanowire height. The short-circuit current of the tandem cell is limited by the smaller of the two. (h) The limiting efficiency of the tandem cell as a function of the nanowire height.

to assess the carrier density, but the precision was limited by the estimation of gate capacitance. Atom probe tomography is another emerging technique to map dopant distribution, which involves sophisticated data reconstruction.[37] The technological issues in doping characterization have hindered the progress of nanowire-on-Si tandem solar cells.

It has been well studied that heavy impurity incorporation results in notable changes in the semiconductor band structure. The random distribution of impurities disturbs the original periodic energy potential. Because the translational symmetry is broken, indirect k-nonconserving transitions become possible. Another important effect is the blue shift of interband transition energy due to band filling in materials with degenerate electron distribution, which is named Burstein−Moss effect.[38,39] These effects on the band structure are directly reflected in the spontaneous emission spectra.

Depending on the impurity concentration, the following two optical transition mechanisms exist:

(i) When translational symmetry is preserved, k-conservation direct band-to-band transition dominates (Figure 3d). The spontaneous emission intensity $I(E)$ can be described as

$$I(E) \propto E^2(E - E_g)^{1/2} \times \left[1 + \exp\left(\frac{m_h^*}{m_e^* + m_h^*} \times \frac{E - E_g}{kT} - \frac{E_F^e - E_g}{kT}\right)\right]^{-1} \times \left\{1 - \left[1 + \exp\left(\frac{-m_e^*}{m_e^* + m_h^*} \times \frac{E - E_g}{kT} - \frac{E_F^h - E_g}{kT}\right)\right]^{-1}\right\} \times |M_{eh}|^2 \quad (1)$$

where the first square term refers to the simple photon density of states in the bulk and the second square root term refers to the density of states of the electron. The next term in the brackets refers to the probability of a state in the conduction band being occupied by an electron based on Fermi−Dirac distribution, while the term in braces is the probability that a corresponding vertical state in the valence band is unoccupied. The last term is the transition matrix element determining the oscillator strength of the transition.

(ii) When translational symmetry is broken, indirect band-to-acceptor transition without k-conservation dominates (Figure 3e). Most photocreated minority carriers thermalize completely before radiative recombination and are energetically situated at

DOI: 10.1021/acs.nanolett.5b03890
Nano Lett. 2015, 15, 7217−7224

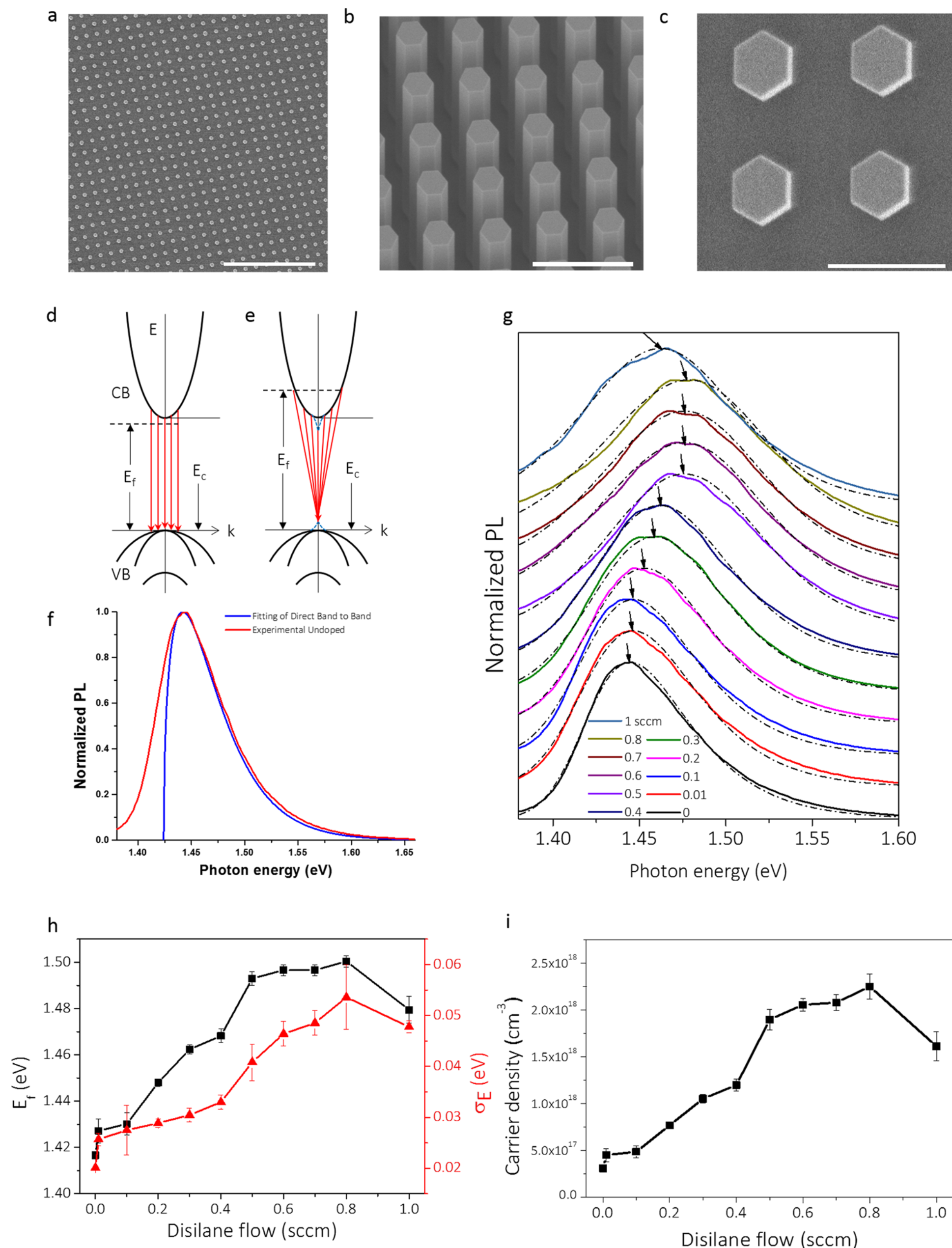

Figure 3. SEM images and characterization of GaAs nanowires. (a−c) SEM images of GaAs nanowires grown on Si(111) substrate using SAG. (a) Top view, scale bar 5 μm. (b) The 30° tilted view, scale bar 1 μm. (c) Magnified top view, scale bar 500 nm. (d) Schematic of *k*-conservation transition in lightly doped and intrinsic semiconductor. (e) Schematic of *k*-nonconservation transition in heavily doped semiconductor due to broken translational symmetry. (f) Theoretical PL spectrum of the intrinsic GaAs nanowire using the direct band-to-band transition mechanism (blue) and experimentally measured spectrum of undoped GaAs nanowire array (red) at room temperature. (g) Normalized room temperature PL spectra of as grown GaAs nanowire arrays on Si. Disilane flow rate is varied between 0 and 1 sccm during the growth. Dotted lines are fitted curves. Curves are intentionally offset for clear view. (h) Fermi level E_f (black) and band tail depth σ_E (red) extracted from photoluminescence study. (i) Carrier density calculated based on the extracted values shown in (h).

the extremum of the band tail. Thus, the PL spectra directly reflects the carrier population in the conduction band

$$I(E) \propto E^2 \times \rho_c \times \left[1 + \exp\left(\frac{E - E_f}{kT}\right)\right]^{-1} \times |M_{eh}|^2 \qquad (2)$$

where ρ_c is the density of states in conduction band. In sufficiently heavily doped semiconductors, the band edge fluctuates spatially. By assuming a Gaussian distribution of the edge fluctuation and the local density of states (DOS) still following a parabolic relationship, Kane gave the analytic form of distorted density of states:[40]

$$\rho_c(E) = \frac{1}{2\pi^2}\left(\frac{2m^*}{\hbar^2}\right)^{3/2} \int_{-\infty}^{E} \sqrt{E - E_c}\,\frac{1}{\sqrt{2\pi}\,\sigma_E} \exp\left[-\frac{1}{2}\left(\frac{E_c}{\sigma_E}\right)^2\right] dE_c \qquad (3)$$

where E_c is the integral variable to take into account all the possible band edge positions and σ_E is the root-mean-square of the energy fluctuation of the band edge.

DOI: 10.1021/acs.nanolett.5b03890
Nano Lett. 2015, 15, 7217−7224

To avoid the donor−acceptor transition that is dominant in low-temperature PL, our study focused on room temperature PL. As grown nanowire arrays were excited by a 532 nm laser with relatively low power intensity (∼1 W cm^{-2}) to avoid optical heating. Room-temperature PL spectra were collected using a 100× objective lens with 0.8 numerical aperture, an 1800 mm^{-1} grating, and a Si charge-couple device (CCD) detector. Figure 3f shows the theoretical PL spectrum of the intrinsic GaAs nanowire using the direct band-to-band transition mechanism (blue) and experimentally measured spectrum of undoped GaAs nanowire array (red) at room temperature. Although no intentional doping was introduced in the undoped sample, the band-to-band transition model spectrum deviates from the experimentally measured spectrum. While the high energy side matches well, a significant tail below the band edge is observed in the experimental spectrum. Because no disilane was supplied, we speculate the band tail is induced by unintentionally incorporated carbon from methyl radicals in TMG during the pyrolysis process[41,42] and is enhanced on As rich surfaces.[43] Figure S1 (see Supporting Information) is the PL spectrum measured from a single undoped nanowire at 4 K. Peak fitting with Lorentzian line shapes was conducted to deconvolve individual peaks. Two dominant peaks are located at 828 and 834 nm, well beyond the band edge at 816 nm. These two peaks have been previously reported to be related to electron-to-carbon acceptor (e, A^0) and carbon donor-to-carbon acceptor (D^0, A^0) transitions.[44]

Given the presence of tail states, we interpreted all the measured PL spectra through the proposed indirect band-to-acceptor transition model. We used eqs 2 and 3 to fit the experimental data using Fermi-level E_f and mean square root of band edge fluctuation σ_E as fitting parameters. E_g is fixed at the nominal band gap of 1.424 eV for GaAs at room temperature. The best fittings are shown in Figure 3g with the black dash-dot fitted curves superimposed on the solid measured curves. All the curves are normalized between 0 and 1 and are offset to better illustrate the line shape evolution with increasing disilane flow rate. The standard deviation for each fitted curve is on the order of 10^{-4}. E_f and σ_E of the best fittings for each doping level are plotted in Figure 3h, based on which the carrier density is calculated as

$$n = \int_{-\infty}^{\infty} \rho_c(E) \times \left[1 + \exp\left(\frac{E - E_f}{kT}\right)\right]^{-1} dE \qquad (4)$$

where ρ_c is defined in eq 3. The calculated carrier density is plotted in Figure 3i. The carrier concentration increases approximately linearly until it reaches about 2 × 10^{18} cm^{-3}. It then saturates with further increases of the disilane flow rates and eventually decreases after it reaches 2.25 × 10^{18} cm^{-3}. Previous studies of Si doped bulk GaAs also found that the carrier density increases linearly up to 3 × 10^{18} cm^{-3} with increasing disilane-to-TMG ratio and the Si atoms are fully ionized as donors.[45] Further increasing the disilane flow rates leads to linearly increased atomic Si concentrations in GaAs while the carrier density tends to saturate. Such a deviation is caused by the self-compensation mechanism of Si given its amphoteric nature.[46,47] Domke et al. atomically resolved various compensation mechanisms in real-space by scanning tunneling microscopy.[47] With increasing Si concentrations, the Si_{Ga} donors are consecutively electrically deactivated by Si_{As} acceptors, Si clusters, and Si_{Ga}−Ga vacancy complexes.

On the basis of the doping information in the GaAs nanowires, we then characterized the transport properties of the proposed n^+-GaAs nanowire/p^+-Si heterojunction. The device schematic is shown in the inset of Figure 4. The Si wafer

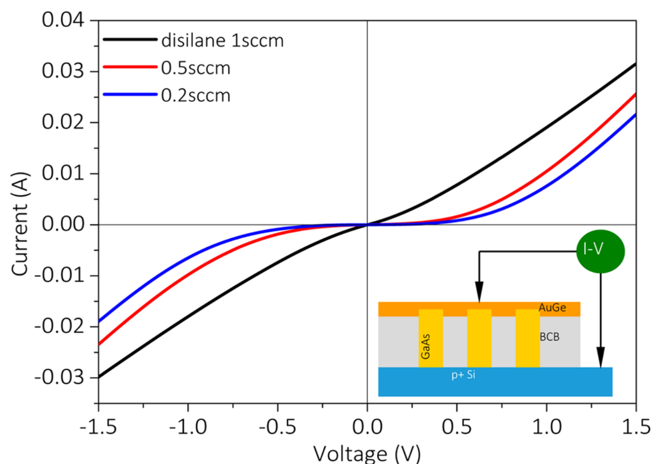

Figure 4. n^+-GaAs/p^+-Si heterojunction characterization. $I-V$ curves of three doping levels, 0.2, 0.5, and 1 sccm, were measured. The former two shows barrier while the latter does not. Inset shows the schematic of the device in measurement.

was implanted with boron ion followed by thermal activation. The doping concentration in the surface layer was around 1 × 10^{21} cm^{-3}. After BCB infiltration, the nanowire arrays were planarized and etched back to expose the tips. Ohmic top contact was formed by depositing AuGe/Ni/Au and rapid thermal annealing. Nanowires doped with 0.2, 0.5, and 1 sccm disilane were studied. From the current (I) versus voltage (V) curves in Figure 4, the 0.2 and 0.5 sccm samples show symmetrical shapes with barriers while the 1 sccm sample shows ohmic behavior. We have seen earlier in Figure 3i that the carrier density for the sample doped with 1 sccm disilane flow rate is lower than that of the sample doped with a 0.5 sccm disilane flow rate. However, the former shows higher current and lower energy barrier when forming a heterojunction with p^+ Si. We believe that the deep acceptor states in GaAs with higher Si concentration effectively reduced the valence band discontinuity between GaAs and Si, lowering the barrier for hole current. More deep level states can also facilitate trap-assisted tunneling process at the heterointerface. We note that the heterojunction of n^+-GaAs/p^+-Si prepared using SAG MOCVD is rather new and has not been fully studied, and whether the low-resistance n^+-GaAs/p^+-Si connecting junction we have made is a tunnel junction deserves further study. The extracted resistance from Figure 4 for the sample doped with 1 sccm disilane flow rate is 50 Ω for a device area of 1 mm × 1 mm, meaning the voltage drop across the heterojunction would be only around 0.01 V for an estimated 20 mA/cm^2 J_{sc} for the tandem cell. Thus, this heterojunction is a good candidate as interconnection for the proposed tandem solar cell architecture.

In order to gain more insight into the performance of the tandem cells, we fabricated and characterized separate Si solar cells and GaAs nanowire solar cells. When characterizing stand-alone Si solar cells, we deposited Ti/Pd/Ag as the front contact and Al as the back contact. Detailed fabrication steps are presented in the Supporting Information. The $J-V$ curves of Si solar cells were measured both in dark and under AM 1.5 G solar spectrum, which give J_{sc} of 26.28 mA/cm^2, V_{oc} of 0.547 V,

DOI: 10.1021/acs.nanolett.5b03890
Nano Lett. 2015, 15, 7217−7224

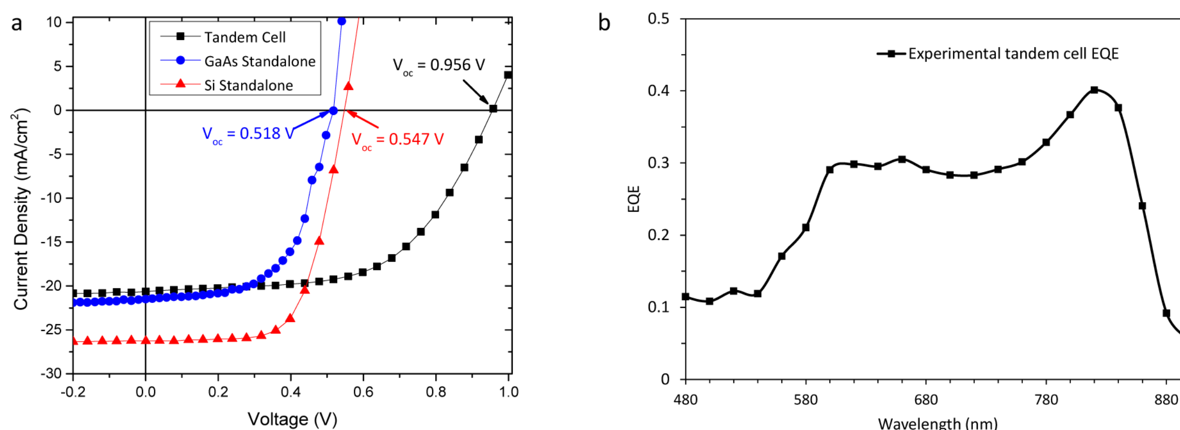

Figure 5. $J-V$ curves and EQE (a) Open circuit voltage addition of the GaAs nanowire-on-Si tandem solar cell. $J-V$ curves of the GaAs nanowire-on-Si tandem solar cell (black), the stand-alone GaAs nanowire cell (blue) and the stand-alone Si cell (red). The arrows indicate the open circuit voltages for each cell, showing an addition of V_{oc} of the tandem cell (0.956 V) from separate stand-alone GaAs nanowire (0.518 V) and stand-alone Si (0.547 V) cells. (b) Experimentally measured EQE of the tandem cell.

fill factor (FF) of 0.658, and overall efficiency of 9.41%. Shunt resistance and series resistance are 8.61 kΩ and 3.24 Ω for a 1 cm^2 cell. Ruling out the effect of shunt and series resistance, the FF is 0.77 and η is 11.03%. The performance is well below that of state-of-the-art commercial Si solar cells due to the lack of optimization in many aspects. To just name a few, no surface texturing was formed to reduce reflection loss, surface passivation layers were not introduced to lower the surface recombination losses at both sides, the doping of emitter layer was high in order to achieve good heterojunction, resulting in short minority lifetime,[48] and the shunt resistance was finite due to the small dimensions of the lab cells. To characterize the top GaAs nanowire cell, we applied the same techniques as in our previous paper[15] to fabricate stand-alone GaAs nanowire cells except that the nanowire heights were modified to be 900 nm. The cells show J_{sc} of 21.50 mA/cm^2, V_{oc} of 0.518 V, FF of 0.581, and η of 6.44%. This short-circuit current density is similar to that of the simulated GaAs subcell in optimal tandem cell structure with 900 nm nanowire height, which verifies that the experimental results are consistent with our simulation.

The final accomplishment was to integrate all essential components and fabricate functioning nanowire-on-Si tandem cells. Following the same steps for Si cell fabrication up to implanted ion activation, we grew a thin segment of GaAs nanowires with 1 sccm disilane on Si bottom cell in order to form low-resistance connecting junction mentioned above. During the growth of GaAs nanowires for the top cell, we controlled the heights of the nanowires to 900 nm to keep them the same as in our stand-alone GaAs nanowire cell. Subsequent steps are described in the Supporting Information to conclude the fabrication. The tandem solar cell performance was measured under AM 1.5 G solar spectrum. Samples were diced into the area with nanowires grown on top (1 mm^2) for fair evaluation. The most efficient tandem cell shows J_{sc} of 20.64 mA/cm^2, V_{oc} of 0.956 V, FF of 0.578, and η of 11.4%. The $J-V$ curves of the stand-alone Si cell, the stand-alone GaAs nanowire cell, as well as the integrated tandem cell are shown in Figure 5a. The open circuit voltages of the stand-alone Si cell (red), the stand-alone GaAs nanowire cell (blue), and the integrated tandem cell (black) are 0.547, 0.518, and 0.956 V respectively, as indicated by arrows and directly compared in Figure 5a. The open circuit voltage of the tandem cell is approximately equal to the summation of the open circuit voltages of the Si and the GaAs nanowire cells. The slight drop in the tandem cell's V_{oc} as compared to the summation could be due to the enhanced surface recombination at the heterointerface for the Si solar cell and nonradiative recombination at heavily doped nanowire root for the GaAs nanowire solar cell. In addition, the J_{sc} of the tandem cell (20.64 mA/cm^2) is very close to the J_{sc} in the simulated current-matching case (19.4 mA/cm^2) in Figure 2e. On the basis of these evidence, we believe the GaAs nanowire subcell and the Si subcell in our tandem cell are connected in series with nearly matched currents.

Furthermore, we also carried out external quantum efficiency (EQE) measurement on the tandem cell. The measured EQE versus wavelength plot is shown in Figure 5b. At wavelength with photon energy smaller than the GaAs bandgap, the GaAs nanowire subcell would not absorb such photons, rendering the current essentially zero, and as expected, the serially connected structure observes a sharp drop in EQE with wavelength larger than ~867 nm. While for a single junction solar cell, the J_{sc} can be calculated by integrating the product of the EQE and AM 1.5 G photon density,[15] we note that for a tandem solar cell, such a calculation would lead to an underestimated value for J_{sc} (see Supporting Information). On the basis of Figure 5b, the integration of the product of EQE and AM 1.5 G photon density results in a value of 7.58 mA/cm^2, which is indeed smaller than the measured J_{sc} of 20.64 mA/cm^2. More details about the EQE study can be found in the Supporting Information.

Although the overall efficiency is still low compared to today's GaAs or Si solar cells, our demonstration of tandem cell behavior through nanowires on a mismatched substrate serves as a starting point and opens up routes for future development and optimization. For example, surface passivation of both Si and GaAs nanowire subcells would allow their individual V_{oc} to approach that of state-of-the-art Si and GaAs solar cells. In our study, a silicon nitride layer was prepared using plasma enhanced chemical vapor deposition to serve as both the growth mask and the front surface passivation layer of the Si solar cell; however, the silicon nitride deposition condition needs to be further tuned and optimized to minimize the dangling bonds on the Si surface. In addition, the back surface of the Si cell was not passivated in our study, which would be another source of recombination loss, and we believe that the

DOI: 10.1021/acs.nanolett.5b03890
Nano Lett. 2015, 15, 7217–7224

passivation of the back Si surface can lead to improved efficiency. Even more important is the surface treatment of GaAs nanowire, as GaAs is known for high density of surface states and the surface-to-volume ratio is very large for nanowire structures. Well-engineered shells with wide band gaps, for example, AlGaAs and InGaP, could be promising candidates.[49,50] Another significant constraint is the short diffusion length in the emitter of the Si solar cell due to the ultrahigh doping. In case one can confine the high doping only to the area underneath the nanowires, both V_{oc} and J_{sc} of the Si cells can be further improved.

To conclude, the work presents the concept of nanowire-on-Si heterostructure involving monolithic integration of lattice-mismatched materials. This is the first demonstration of tandem solar cells using top GaAs nanowire array cells grown on lattice-mismatched bottom Si cells, which not only shows current matching between individual subcells but also achieves low-resistance ohmic behavior across the heterojunction. The tandem cells observe voltage addition of GaAs nanowire and Si cells showing V_{oc} up to 0.956 V and efficiency of 11.4%. The presented structure opens up great opportunities for future nanowire-based, low-cost, and high-efficiency multijunction solar cells.

■ ASSOCIATED CONTENT

Supporting Information

The Supporting Information is available free of charge on the ACS Publications website at DOI: 10.1021/acs.nanolett.5b03890.

> Details on nanowire growth, Si solar cell fabrication, tandem solar cell fabrication, the PL spectra of a single undoped GaAs nanowire, and the EQE study are provided. (PDF)

■ AUTHOR INFORMATION

Corresponding Authors

*E-mail: (C.Z.) chongwuz@usc.edu.

*E-mail: (P.D.D.) dapkus@usc.edu.

Author Contributions

M.Y. and S.C. contributed equally.

Notes

The authors declare no competing financial interest.

■ ACKNOWLEDGMENTS

This material is based upon work supported as part of the Center for Energy Nanoscience (CEN), an Energy Frontier Research Center (EFRC) funded by the U.S. Department of Energy, Office of Science and Office of Basic Energy Sciences under Award Number DE-SC0001013. Computing resources were provided by the USC Center for High Performance Computing and Communications. M.Y. was funded by USC Provost's Ph.D. Fellowship. The authors thank UCSB Nanofabrication facility and Brian Thibeault for providing DUV stepper lithography service and development.

■ REFERENCES

(1) Shockley, W.; Queisser, H. J. *J. Appl. Phys.* **1961**, *32*, 510−519.
(2) Henry, C. H. *J. Appl. Phys.* **1980**, *51*, 4494−4500.
(3) Bedair, S. M.; Lamorte, M. F.; Hauser, J. R. *Appl. Phys. Lett.* **1979**, *34*, 38−39.
(4) Virshup, G. F.; Chung, B. C.; Werthen, J. G. *20th IEEE Photovoltaic Specialists Conference*, Las Vegas, NV, September 26−30, 1988; pp 441−445.
(5) King, R. R.; Law, D. C.; Edmondson, K. M.; Fetzer, C. M.; Kinsey, G. S.; Yoon, H.; Sherif, R. A.; Karam, N. H. *Appl. Phys. Lett.* **2007**, *90*, 183516.
(6) Green, M. A.; Emery, K.; Hishikawa, Y.; Warta, W.; Dunlop, E. D. *Prog. Photovoltaics* **2014**, *22*, 701−710.
(7) Dimroth, F.; Grave, M.; Beutel, P.; Fiedeler, U.; Karcher, C.; Tibbits, T. N. D.; Oliva, E.; Siefer, G.; Schachtner, M.; Wekkeli, A.; Bett, A. W.; Krause, R.; Piccin, M.; Blanc, N.; Drazek, C.; Guiot, E.; Ghyselen, B.; Salvetat, T.; Tauzin, A.; Signamarcheix, T.; Dobrich, A.; Hannappel, T.; Schwarzburg, K. *Prog. Photovoltaics* **2014**, *22*, 277−282.
(8) Tian, B. Z.; Zheng, X. L.; Kempa, T. J.; Fang, Y.; Yu, N. F.; Yu, G. H.; Huang, J. L.; Lieber, C. M. *Nature* **2007**, *449*, 885−889.
(9) Goto, H.; Nosaki, K.; Tomioka, K.; Hara, S.; Hiruma, K.; Motohisa, J.; Fukui, T. *Appl. Phys. Express* **2009**, *2*, 035004.
(10) Tomioka, K.; Tanaka, T.; Hara, S.; Hiruma, K.; Fukui, T. *IEEE J. Sel. Top. Quantum Electron.* **2011**, *17*, 1112−1129.
(11) Hu, S.; Chi, C. Y.; Fountaine, K. T.; Yao, M. Q.; Atwater, H. A.; Dapkus, P. D.; Lewis, N. S.; Zhou, C. W. *Energy Environ. Sci.* **2013**, *6*, 1879−1890.
(12) Mariani, G.; Scofield, A. C.; Hung, C. H.; Huffaker, D. L. *Nat. Commun.* **2013**, *4*, 1497.
(13) Cui, Y. C.; Wang, J.; Plissard, S. R.; Cavalli, A.; Vu, T. T. T.; van Veldhoven, R. P. J.; Gao, L.; Trainor, M.; Verheijen, M. A.; Haverkort, J. E. M.; Bakkers, E. P. A. M. *Nano Lett.* **2013**, *13*, 4113−4117.
(14) Wallentin, J.; Anttu, N.; Asoli, D.; Huffman, M.; Aberg, I.; Magnusson, M. H.; Siefer, G.; Fuss-Kailuweit, P.; Dimroth, F.; Witzigmann, B.; Xu, H. Q.; Samuelson, L.; Deppert, K.; Borgstrom, M. T. *Science* **2013**, *339*, 1057−1060.
(15) Yao, M. Q.; Huang, N. F.; Cong, S.; Chi, C. Y.; Seyedi, M. A.; Lin, Y. T.; Cao, Y.; Povinelli, M. L.; Dapkus, P. D.; Zhou, C. W. *Nano Lett.* **2014**, *14*, 3293−3303.
(16) Huang, N. F.; Lin, C. X.; Povinelli, M. L. *J. Opt.* **2012**, *14*, 024004.
(17) Huang, N. F.; Lin, C. X.; Povinelli, M. L. *J. Appl. Phys.* **2012**, *112*, 064321.
(18) Wen, L.; Zhao, Z. F.; Li, X. H.; Shen, Y. F.; Guo, H. M.; Wang, Y. Q. *Appl. Phys. Lett.* **2011**, *99*, 143116.
(19) Madaria, A. R.; Yao, M. Q.; Chi, C. Y.; Huang, N. F.; Lin, C. X.; Li, R. J.; Povinelli, M. L.; Dapkus, P. D.; Zhou, C. W. *Nano Lett.* **2012**, *12*, 2839−2845.
(20) Lin, C. X.; Povinelli, M. L. *Opt. Express* **2009**, *17*, 19371−19381.
(21) Kelzenberg, M. D.; Boettcher, S. W.; Petykiewicz, J. A.; Turner-Evans, D. B.; Putnam, M. C.; Warren, E. L.; Spurgeon, J. M.; Briggs, R. M.; Lewis, N. S.; Atwater, H. A. *Nat. Mater.* **2010**, *9*, 239−244.
(22) LaPierre, R. R. *J. Appl. Phys.* **2011**, *110*, 014310.
(23) Gudiksen, M. S.; Lauhon, L. J.; Wang, J.; Smith, D. C.; Lieber, C. M. *Nature* **2002**, *415*, 617−620.
(24) Glas, F. *Phys. Rev. B: Condens. Matter Mater. Phys.* **2006**, *74*, 121302(R).
(25) Sburlan, S.; Dapkus, P. D.; Nakano, A. *Appl. Phys. Lett.* **2012**, *100*, 163108.
(26) Chuang, L. C.; Moewe, M.; Chase, C.; Kobayashi, N. P.; Chang-Hasnain, C.; Crankshaw, S. *Appl. Phys. Lett.* **2007**, *90*, 043115.
(27) Ertekin, E.; Greaney, P. A.; Chrzan, D. C.; Sands, T. D. *J. Appl. Phys.* **2005**, *97*, 114325.
(28) Tobias, I.; Luque, A. *Prog. Photovoltaics* **2002**, *10*, 323−329.
(29) Hu, Y.; Li, M.; He, J. J.; LaPierre, R. R. *Nanotechnology* **2013**, *24*, 065402.
(30) Li, M.; Hu, X. H.; Ye, Z.; Ho, K. M.; Cao, J. R.; Miyawaki, M. *Opt. Lett.* **2006**, *31*, 3498−3500.
(31) Reference Solar Spectral Irradiance: Air Mass 1.5 Spectra. http://rredc.nrel.gov/solar/spectra/am1.5 (April 28th, 2015).
(32) Olson, J. M.; Kurtz, S. R.; Kibbler, A. E.; Faine, P. *Appl. Phys. Lett.* **1990**, *56*, 623−625.

DOI: 10.1021/acs.nanolett.5b03890
Nano Lett. 2015, 15, 7217−7224

(33) Bertness, K. A.; Kurtz, S. R.; Friedman, D. J.; Kibbler, A. E.; Kramer, C.; Olson, J. M. *Appl. Phys. Lett.* **1994**, *65*, 989−991.
(34) Casadei, A.; Krogstrup, P.; Heiss, M.; Rohr, J. A.; Colombo, C.; Ruelle, T.; Upadhyay, S.; Sorensen, C. B.; Nygard, J.; Morral, A. F. I. *Appl. Phys. Lett.* **2013**, *102*, 013117.
(35) Bessire, C. D.; Bjork, M. T.; Schmid, H.; Schenk, A.; Reuter, K. B.; Riel, H. *Nano Lett.* **2011**, *11*, 4195−4199.
(36) Yang, T.; Hertenberger, S.; Morkotter, S.; Abstreiter, G.; Koblmuller, G. *Appl. Phys. Lett.* **2012**, *101*, 233102.
(37) Perea, D. E.; Hemesath, E. R.; Schwalbach, E. J.; Lensch-Falk, J. L.; Voorhees, P. W.; Lauhon, L. J. *Nat. Nanotechnol.* **2009**, *4*, 315−319.
(38) Burstein, E. *Phys. Rev.* **1954**, *93*, 632−633.
(39) Moss, T. S. *Proc. Phys. Soc., London, Sect. B* **1954**, *67*, 775−782.
(40) Kane, E. O. *Phys. Rev.* **1963**, *131*, 79−88.
(41) Kushibe, M.; Eguchi, K.; Funamizu, M.; Ohba, Y. *Appl. Phys. Lett.* **1990**, *56*, 1248−1250.
(42) Kuech, T. F.; Redwing, J. M. *J. Cryst. Growth* **1994**, *145*, 382−389.
(43) Kuech, T. F.; Veuhoff, E. *J. Cryst. Growth* **1984**, *68*, 148−156.
(44) Bose, S. S.; Lee, B.; Kim, M. H.; Stillman, G. E.; Wang, W. I. *J. Appl. Phys.* **1988**, *63*, 743−748.
(45) Shimazu, M.; Kamon, K.; Kimura, K.; Mashita, M.; Mihara, M.; Ishii, M. *J. Cryst. Growth* **1987**, *83*, 327−333.
(46) Druminski, M.; Wolf, H.-D.; Zschauer, K.-H.; Wittmaack, K. *J. Cryst. Growth* **1982**, *57*, 318−324.
(47) Domke, C.; Ebert, P.; Heinrich, M.; Urban, K. *Phys. Rev. B: Condens. Matter Mater. Phys.* **1996**, *54*, 10288−10291.
(48) Green, M. A. *Prog. Photovoltaics* **2009**, *17*, 183−189.
(49) Chang, C. C.; Chi, C. Y.; Yao, M. Q.; Huang, N. F.; Chen, C. C.; Theiss, J.; Bushmaker, A. W.; LaLumondiere, S.; Yeh, T. W.; Povinelli, M. L.; Zhou, C. W.; Dapkus, P. D.; Cronin, S. B. *Nano Lett.* **2012**, *12*, 4484−4489.
(50) Huang, N. F.; Povinelli, M. L. *IEEE J. Photovolt.* **2014**, *4*, 1511−1517.

DOI: 10.1021/acs.nanolett.5b03890
Nano Lett. 2015, 15, 7217−7224